Plastic shrinkage of mortars cured with a paraffin-based compound – Bimodal neutron/X-ray tomography study

Mateusz Wyrzykowski [a,*], Sadegh Ghourchian [a], Beat Münch [a], Michele Griffa [a], Anders Kaestner [b,*], Pietro Lura [a,c]

[a] Empa, Swiss Federal Laboratories for Materials Science and Technology, Dübendorf, Switzerland
[b] Paul Scherrer Institute (PSI), Villigen, Switzerland
[c] Institute for Building Materials (IfB), ETH Zurich, Zurich, Switzerland

ARTICLE INFO

ABSTRACT

Early-age drying (immediately after casting) of mortars and the corresponding plastic shrinkage were studied using bimodal neutron/X-ray computed tomography. This novel, correlative 3D imaging mode enabled studying simultaneously and without any source of spurious perturbation the water migration and loss processes together with the corresponding deformations due to plastic shrinkage. Bimodal imaging opens up new possibilities for studying dynamic processes of coupled water transport and deformations in porous solids. The measurements were carried out on model systems (cylindrical mortar specimens with height of 19 mm). The study focused on the effect of a paraffin-based curing compound. Our results confirm that when the curing compound was applied directly onto the drying surface in a sufficient amount, both the evaporation rate and the rate of vertical displacement (settlement) were substantially reduced. The results shed a new light on the mechanisms of plastic shrinkage and the action of curing compounds.

1. Introduction

The evaporation of water from fresh concrete after placement and until the concrete becomes solid is responsible for large deformations, referred to as plastic shrinkage [1–5]. In concrete structures, plastic shrinkage is in most cases restrained by geometrical constraints, the subgrade, reinforcement, etc. This leads to the buildup of restraint stresses and may result in cracking [3,6]. Plastic shrinkage cracking can seriously impair the durability of concrete, mainly because early-age cracks further act as pathways for aggressive media that accelerate reinforcement corrosion [7,8]. The negative consequences of early-age drying can be effectively avoided with proper curing of concrete after casting [9].

Different methods have been proposed for curing of concrete and reduction of plastic shrinkage cracking. The most straightforward and traditional methods are the so-called active solutions aimed at limiting evaporation after placing, e.g. by covering of drying surfaces with wet-burlaps, plastic sheets or spraying them with water [10,11]. Another class of methods particularly convenient in practice, the so-called passive solutions, relies on modifying the concrete at the stage of mixing.

Here belong shrinkage reducing admixtures (SRA) based on different types of surfactants. SRA reduce the surface tension of the pore water [12,13]. Hence they reduce the capillary suction arising in the pores of drying concrete [14]. This results in reduction of evaporation, plastic shrinkage and cracking of fresh concrete, e.g. [14–18].

Another mitigation strategy is based on limiting the early age evaporation from the concrete by sealing the drying surfaces with liquid chemical compounds, often referred to as membrane curing [10,19–22]. Membrane curing was introduced in the US already in the 1940s as a wartime substitute for traditional curing (burlap covering or water ponding) as it required less labor and supervision [10,21,22]. Membrane curing soon proved to be in many cases more efficient than traditional wet curing and became a standardized solution [23].

The curing compounds to form membranes can be water emulsions or solutions incorporating e.g. resins, chlorinated rubber, bitumen, linseed oil or paraffin wax [11,19,24–26]. Sometimes, white pigments can be additionally used, aimed at reducing the heating of the cured surfaces from solar radiation [10,23]. Optionally, fugitive dyes can be also added to facilitate assessing whether the concrete surface is covered uniformly [21]. Such dyes should decompose and fade after few hours of

exposure to sunlight.

The membranes can be used in two ways. Traditionally, curing compounds were sprayed or brushed directly on the drying surfaces shortly after casting (hence, active solution). A more recent method is adding the curing compound (usually in the form of water dispersion) as admixture to a concrete mix (hence, it is a passive solution as defined above). In the latter case, the designated mechanism is as follows [14]: the dispersion containing the compound is expected to migrate to the drying surface during the early stages of drying and the curing compound is expected to accumulate there as water evaporates. Both methods of delivery proved to be successful in limiting the evaporation in numerous laboratory and field studies [14,17,26]. From a practical point of view, adding the curing compound during concrete mixing is preferred, as it requires no additional actions after concrete placing. In addition to requiring labor, applying the curing compound on the concrete surface needs to be timely and accurate, as any delay or a non-uniform layer could result in cracking.

This paper is devoted to an experimental investigation of membrane curing with a paraffin-based water dispersion in mortars exposed to drying directly after casting. To this end, a commercially available liquid curing compound was either mixed into the mortar (as recommended by the producer) or poured after casting on the top surface.

Plastic shrinkage and the corresponding cracking of concrete have been studied experimentally most often on relatively large specimens (exposed surfaces of dozens of centimeters across, depth of several centimeters), that make the observation of surface cracking possible, e.g. [2,16,17,27–30]. In order to overcome the limitation of the methods where cracks can be evaluated only optically once they reach a (visible) surface, Ghourchian et al. [6] recently employed X-ray radiography on a mortar specimen to follow up crack initiation directly at the location of a stress riser below the concrete surface. That study was aided with modelling based on poromechanics (see also [31]) and brittle failure models.

Bentz et al. studied water content changes in fresh cement pastes and mortars exposed to drying with conventional (absorption-based) X-ray radiography [32,33]. The spatial resolution reported in those studies was 0.2 mm and the plastic shrinkage deformations were not measured. Due to the features described later in this section, neutron imaging offers better resolution for water content changes in cement-based materials during drying than X-ray imaging, e.g. [34–37]. Mortars either with presaturated lightweight aggregates or SRA undergoing plastic shrinkage were studied with neutron tomography in [38]. However, while changes of water content in the LWA grains and in the mortars could be followed, the deformations (shrinkage) of the mortars could not be resolved due to limited resolution and contrast (the voxel size was larger than).

In order to overcome the contrast and/or resolution limitations of the previous studies, in the present study combined neutron/X-ray tomography implemented at the ICON beamline of the Laboratory for Neutron Scattering and Imaging, Paul Scherrer Institute (PSI), Villigen, Switzerland was used. Such bimodal tomographic measurements were carried out on model mortar specimens (cylindrical specimens, Ø18 mm, h = 19 mm) during their exposure to drying right after casting.

Compared to the previous studies with either X-ray or neutron imaging, the two chosen 3D imaging modalities could profit from the sensitivity to distinct material phases and features [39]. Thanks to the large neutron interaction (primarily scattering) cross-section of hydrogen [40], neutron tomography is a particularly powerful imaging method for studying spatial and temporal distribution of water in porous media [41], including cementitious materials [42]. In fact, in the neutron tomography measurements presented in this paper, about 85% of signal was due to water in the mortars. On the other hand, conventional X-ray tomography relying mainly on photoelectric absorption-based contrast, allows better detection of the solids in the mortars. Both techniques were applied simultaneously at the same experimental facility, for tomography of fresh mortars. Neutron tomography enabled

visualizing and quantitatively characterizing the migration of water and curing compound. Shrinkage was followed with both techniques. However, X-ray tomography allowed detecting primarily the solid part, whereas neutron tomography also the layer of water or curing compound accumulated on the top surface.

In addition to the advantages stemming from the combined sensitivities, the bimodal *simultaneous* tomography has significant advantages compared to the case where the specimen is moved between separate neutron and X-ray facilities. The first advantage is achieving almost perfect synchronicity of the X-ray and neutron measurements while significantly increasing the temporal sampling frequency for the acquisitions with both tomography modalities. This is in particular important for the time scales characteristic of the dynamic processes accompanying early age drying, i.e. minutes to several minutes. Even more important from the point of view of the drying process is that moving a sample between different setups would mean altering the drying conditions during and in between the measurements. Such disturbance could be avoided with the bimodal imaging.

The results presented here offer insights into the mechanisms of early age drying and shrinkage as well as into the ways in which these processes can be controlled with curing compounds. Further, the study shows new possibilities for studying dynamic water transport and deformation processes in porous media, like cement-based materials, soils, wood, etc. by means of bimodal, simultaneous neutron/X-ray imaging.

2. Materials and methods

2.1. Mortars mixing and drying

Ordinary Portland cement CEM I 42.5N (Jura, Switzerland) was used. The composition of the cement, measured by X-ray fluorescence (XRF) was the following (by mass): CaO 63%, SiO_2 19%, Al_2O_3 4.6% Fe_2O_3 3.2%, MgO 2.0%, SO_3 3.2%, K_2O 0.81%, Na_2O 0.22%.

Alluvial sand from Switzerland with well-rounded particles (sieved to sizes 0.25–1 mm) was used as aggregate. The aggregates had density of 2.65 g/cm^3 and occupied about 45% of the volume in the mortars. Deionized water was used as mixing water. The curing compound tested was a commercial product (Masterlife IC100 by BASF) based on white paraffin-in-water dispersion with nominal solid content of 40 ± 2% and density of 0.95 g/cm^3.

All mortars had the same water-to-cement ratio (w/c) of 0.5. Four mortar specimens were tested:

- two specimens with reference mortar (REF and REF-duplicate, obtained from separate mixings),
- a single specimen of a mortar with curing compound incorporated during mixing (CURE-MIX),
- a single specimen of a mortar with curing compound spread onto the surface (CURE-SURF).

All the tests were carried out within 3.5 d (starting with the REF specimen and finishing with the REF-duplicate specimen).

The CURE-SURF specimen was made of the reference mortar (mixed independently), with 0.1839 g of the curing compound spread uniformly over the whole top surface of the sample using a pipette. This amount corresponded to an average thickness of approximately 0.8 mm and a consumption of curing compound of 0.72 kg per m^2 of surface.

The CURE-MIX mortar had the same composition as the REF mortar, except for the curing compound added at 1.5% by mass of cement (maximum dosage recommended by the producer). The water content in the curing compound (assumed as 60% by mass) was accounted as part of the mixing water (hence, the total water content was the same as in the reference mortar). The mix compositions are presented in Table 1.

The mortars were mixed for 2 min in small batches (300 ml) in a vacuum mixer (Twister Evolution by Renfert) at 450 rpm speed. After

Table 1

Mix compositions in [kg/m^3] of the tested mortars REF and CURE-MIX. Note that the CURE-SURF specimen was filled with the REF mortar. The air content (small due to vacuum mixing) was not considered in the mix composition.

Mortar	Cement CEM I 42.5N	Sand 0.25–1.0 mm	Deionized water	Curing compound
REF	670	1200	335	–
CURE-MIX	670	1200	329	10

about 3 min mixing, the fresh mortars were cast in glass-reinforced PTFE cylindrical containers with internal dimensions: diameter 18 mm, height 19 mm, and wall thickness 1 mm, see Fig. 1. Similarly as in the previous studies [38,43,44], the PTFE was chosen for the containers mainly for the following reasons: it has a relatively low neutron interaction cross-section (lower than a mortar), it does not react with cement solution, and finally, it exerts little friction against the deformations of the mortar. Further, the diameter-to-height ratio of the specimens (here about 1) should guarantee that the bleeding is little affected by the wall-effect according to [45] (where a minimum ratio of 0.24 was suggested).

Within 5–10 min from casting, the samples were placed on the rotating stage of the tomography setup and the measurements started before 15 min from casting. During the experiments, drying of the top surfaces was accelerated by means of air blown by a small fan (Ø75 mm, commonly used for cooling computer components) placed at approximately 20 cm from the samples. The air speed measured with a hot-wire anemometer probe near the samples was ~1 m/s. The temperature in the experiment room was 27 ± 0.5 °C and the relative humidity (RH) was in the range 35–45%RH.

The masses of the samples were determined before (directly after casting) and after each tomography measurement as well as later on. After tomography, the samples were stored in the vicinity of the rotating stage. This means that they remained exposed to similar drying conditions regarding temperature and RH, yet it was possible that the air speed was lower compared to that maintained during the tomography.

2.2. Bimodal neutron/X-ray tomography

Tomography with neutrons took place at the ICON (Imaging with COld Neutrons) beamline [46] fed from the Swiss Spallation Neutron Source (SINQ) at PSI. ICON offers, as an additional plugin module, an X-ray tomograph based upon a micro-focus, laboratory-scale X-ray source [47]. With such plugin, a specimen can be irradiated also by an X-ray beam, with propagation direction (optical axis) at a slant angle

Fig. 1. Mortar specimen in a Ø18 mm PTFE container (here shown the CURE-SURF specimen with paraffin-based curing compound on the upper surface).

compared with the neutron beam's one (see Supplementary Materials, Fig. S1). In the present experiments, the specimens were irradiated by both the neutron and the X-ray beams simultaneously, i.e. the tomography measurements were carried out during the same time intervals.

A 3D dataset from tomography, a *tomogram*, is obtained through an algorithmic process called *reconstruction* from a number of 2D images, the *radiographs*, acquired in consecutive projections over a certain angle range around an object (here in the range 0–360°), e.g. [48]. One bimodal radiography took 30–40 s, which included X-ray and neutron images acquisition and storage on disk and rotation of the specimen stage to the next position. For each tomogram, a series of such steps is required to collect a sufficient number of radiographs. Hence, a tomogram referring to a certain state in time of a specimen requires that the specimen does not change (significantly) during the time span of the data acquisition. Otherwise, if the dynamic processes, e.g. shrinkage or water transport, occur on shorter time scales than the acquisition, strong motion artifacts appear in the reconstructed tomogram [49]. A minimization of the acquisition time is sought, but it typically leads to a lower signal-to-noise ratio and lower spatial resolution of the final tomograms. Hence, a trade-off between the temporal and spatial resolutions needs to be found while fixing the number of radiographs used in the reconstruction process. The problem becomes especially non-trivial when the time scales of the investigated processes are not well known a priori. To address this issue, one acquisition protocol for the so-called dynamic tomography (tomography with a changing specimen) was used. It allowed reducing motion artifacts in tomograms from under-complete datasets [50]. In a conventional tomography, a sample is irradiated at different angles and the consecutive rotations proceed in a sequence with a constant (small) angle interval in the range 0–360°. Hence, a relatively large number of radiographs (and a long time) is necessary to cover the full angle range. The basic idea of the dynamic tomography method used here is that the range 0–360° is sampled in a rather sparse and homogeneous way in which the difference between one element of the rotational angle sequence and the next one is always close to 90°. Such angle pairs proceed according to the golden ratio sequence [50]. The fact that even for a small number of consecutive radiographs the orientation angle sequence spans the needed range within 360° allows performing tomographic reconstruction, albeit with smaller spatial resolution and more reconstruction artifacts. Most importantly, using such rotation sequence, it is possible a posteriori, i.e., after the end of the experiment, to select only a subset of radiographs for the reconstruction of each tomogram in the time series. Hence, the time resolution of the reconstructed tomograms can be adjusted to meet the specific characteristic times of a physical process that needs to be followed in the experiment.

More details about the bimodal tomographic acquisitions at the ICON beamline are reported in Section S1 of the Supplementary Materials.

2.3. CT data processing

Each reconstructed tomogram, of either type (neutron or X-ray), consists of a stack of 2D images (tomographic slices). Each slice represents a planar cross-section of the mortar specimen in the XY plane (the horizontal plane) at a given height along the vertical Z axis (approximately parallel to the rotation axis of the stage and the symmetry axis of the cylindrical specimen) (see Supplementary Materials, Fig. S1). The slices are spaced along the Z axis at a distance corresponding to the voxel size. The voxel sizes in the reconstructed tomograms were equal to 53 μm and 38 μm, for the neutron and X-ray measurements, respectively. The effective spatial resolution of the tomograms varied depending on the tomogram type and on the sub-set of raw data used for the tomographic reconstruction, i.e., on the tomographic temporal resolution. Although a unique spatial resolution value cannot be precisely estimated, the range 100–150 μm should cover the actual values for the distinct tomograms with distinct temporal resolutions.
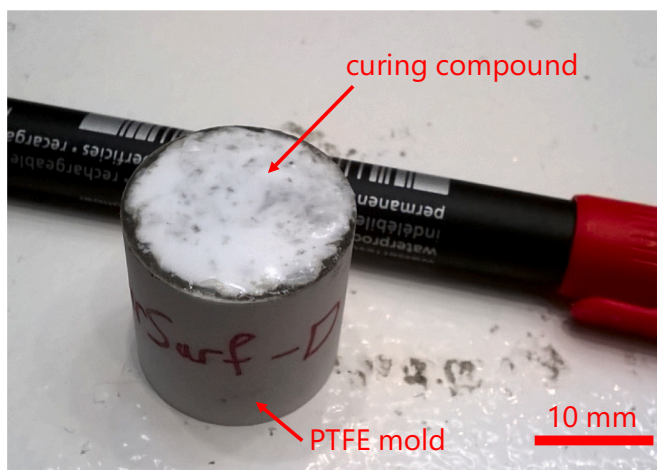
The tomograms were reconstructed using different numbers of radiographs, from 16 to 64 only. This very low number of radiographs allowed to achieve sufficient image quality thanks to the dynamic tomography method described in the previous section. Such subsets of radiographs encompassed acquisition times (temporal resolution) from 9 to 36 min, respectively. The time interval between the consecutive reconstructed tomograms was from 4.5 to 18 min, respectively. This means that any two consecutive tomograms were overlapping in time by half of their acquisition time. The nominal times corresponding to different tomograms used in the presentation of the results represent the starting projection of that tomogram. More details on the data processing algorithm are presented in the Supplementary Materials, Section S2.

The quantification of water content changes based on neutron data was done as follows.

The signal (voxel value) in different points (voxels) in the neutron tomograms is an approximation of the neutron linear attenuation coefficient μ [cm^{-1}] [40]. For a heterogeneous material like mortar, the attenuation coefficient of a given region is approximately the sum of coefficients of different components present in that region, e.g. cement, aggregates, and, most importantly here, *water*. It should be stressed here that the voxel size is smaller than the characteristic aggregate size (0.25–1 mm) or large air void size (few hundreds of μm) in a mortar. Hence, as long as the considerations discussed here theoretically are valid at the level of single voxels, it needs to be considered that summing up attenuation coefficients becomes meaningful only for larger regions. Consequently, the calculation as used here requires that the signal changes be integrated over the whole volume of the (deforming) specimen. This is necessary not only due to the characteristic scale of the features in a mortar mentioned previously, but primarily due to the relatively large deformations of a mortar during plastic shrinkage. Otherwise, considering the signal changes in a certain point in space individually would require following not only water migration within the mortar but also (non-negligible) strains of the mortar itself.

By assuming that the change of attenuation coefficient in the whole volume of a mortar specimen is only due to water migration from that volume (drying), and knowing the contributions of different mortar components to the initial (i.e. before drying) neutron attenuation of the specimen, one can relate the voxel value changes to the changes of mass of water of the specimen.

The theoretical linear attenuation coefficients were calculated for the mortars as sums of coefficients for dry cement, aggregates, water, and paraffin where present, see also [38,43,44]. When considering a molecular compound/material phase, a linear combination of neutron interaction cross-sections of distinct nuclei (after [40,51]), whose coefficients are numerical volumetric density values, are computed to provide the linear attenuation coefficient values μ in units of cm^{-1} (see Eq. (S.4) of Section S3 in the Supplementary Materials). Such values are then combined together, again with a linear combination, to provide the linear attenuation coefficient of a composite material (Eq. (S.3) in Section S3 of the Supplementary Materials).

In the estimations, the oxide composition of the cement given in Section 2.1 was used and the aggregates were assumed to be composed of a single mineral phase, calcium carbonate. Note that any divergence from these assumptions would have a negligible impact on the final evaluation, since the neutron linear attenuation coefficient of the mortar is dominated by that of water. For the paraffin in the curing compound, the formula $C_{20}H_{42}$ was assumed. Also here, the effect on the evaluations was small despite the high neutron attenuation of paraffin, due to the small amount of the curing compound in the mortar CURE-MIX (0.4% by volume, 1.4% by contribution to the voxel value, see Table S1 in Section S3 of the Supplementary Materials).

The theoretical neutron linear attenuation coefficient of the reference mortar after mixing was μ_n=1.438 cm^{-1} (note that the CURE-SURF sample had mortar with the same composition as the REF mortar). The mortar with mixed-in curing compound CURE-MIX had a slightly higher theoretical coefficient, μ_n=1.452 cm^{-1}, due to the high content of hydrogen in the paraffin. The theoretical fraction due to water in the total voxel value was estimated as 0.857 and 0.845 for the REF and CURE-MIX mortars, respectively. For details of the calculation see the Supplementary Materials, Section S3.

3. Results

3.1. Tomography

In Figs. 2 and 3, the vertical center cross-sections of the mortar samples (orthogonal views in the central parts of the 3-D tomograms, XZ plane) at two distinct time points during drying are presented for the CURE-SURF mortar, both for the X-ray and neutron tomograms, respectively. The tomograms at the earlier times (15 min from casting) were obtained with higher tomographic temporal resolution (9 min, with only 16 sequential radiographs used per reconstruction) to follow the rapid initial drying and settlement in the mortars. The tomograms at later times (after about 5 h) were obtained with lower temporal resolution (36 min, with 64 radiographs per reconstruction) but higher spatial resolution. The higher spatial resolution in the tomograms at later times can be clearly recognized, both for the X-ray and the neutron tomograms, by the lower blurring at the boundaries between the mold and the surrounding empty space or mortar and on the interfaces of large pores visible in the central part of the mortar specimen.

Thanks to the high attenuation of the X-ray beam by the solids in the mortars, the X-ray data was used solely for following the deformations of the mortar, while the voxel values in different regions of the mortar obtained with X-rays were relatively constant. On the contrary, the neutron images delivered also important data based on the changes of voxel values in the mortars.

The deformations and voxel values are highly inhomogeneous in the mortars, primarily due to the presence of aggregates occupying 45% by volume of the mortars, and to a lesser extent due to large air voids. Although neat cement pastes would surely offer more homogenous voxel values, the study was carried out on mortars as model systems emulating concrete, specifically in order to study plastic shrinkage with aggregates. In order to cope with the high spatial inhomogeneity of the deformations and voxel values in the mortars, voxel value averages in semi circles around the central vertical axis of the specimens (cylindrical averages) were used in further quantifications. This still enabled resolving horizontal and vertical variability of voxel values or deformations of the samples, while smoothing the scatter due to intrinsic inhomogeneity of the mortars and of the imaging method. The cylindrically averaged tomograms of different mortars at different times for the neutron data are presented in the Supplementary Materials, Section S4, Fig. S2.

To better visualize the pattern of drying over time, the differences between the cylindrically averaged initial tomograms (at 15 ± 1 min from casting) and those at later ages (60, 120, 180 and 340 min), so called difference images, are presented for the different mortars in Figs. 4-6. In these figures, the color scale expressing the change in the neutron attenuation coefficient was cropped at 0.0 and 0.8 cm^{-1}. The lower bound means that negative values corresponding to mass gain were neglected. They were assumed as due to noise because their absolute values were small (up to 0.05 cm^{-1}) and occurred only at single spots within the bulk of the specimens. One meaningful exception is the significant voxel value gain (negative values in difference images) due to accumulation of the paraffin on the top surface in the CURE-SURF mortar (see Supplementary Materials, Fig. S1). The upper cropping bound, 0.8, was chosen because above this threshold the loss of neutron attenuation was due to displacement of the whole mortar body rather than loss of water from within the mortar. It should be stressed that the color scale cropping was only done for the sake of visualization, whereas no cropping was used in the actual quantifications.

The first feature visible in the difference images in Figs. 4-6 (and in the cylindrically averaged tomograms in Fig. S2 in the Supplementary
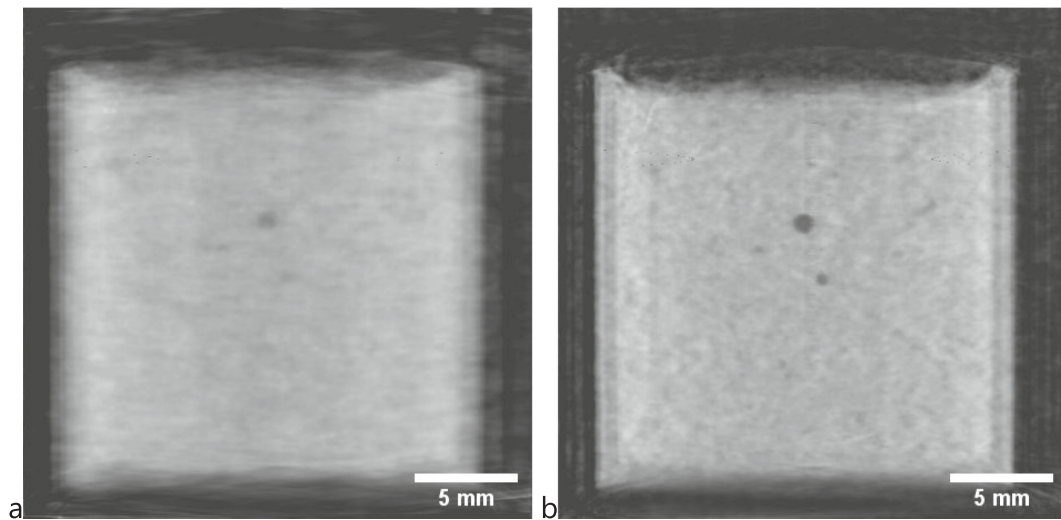
Fig. 2. Vertical cross-section through the center of the cylindrical sample of the CURE-SURF mortar obtained from the X-ray tomograms at different times from casting: a) $t = 15$ min (temporal resolution of 9 min), b) t = ~320 min (temporal resolution of 36 min).
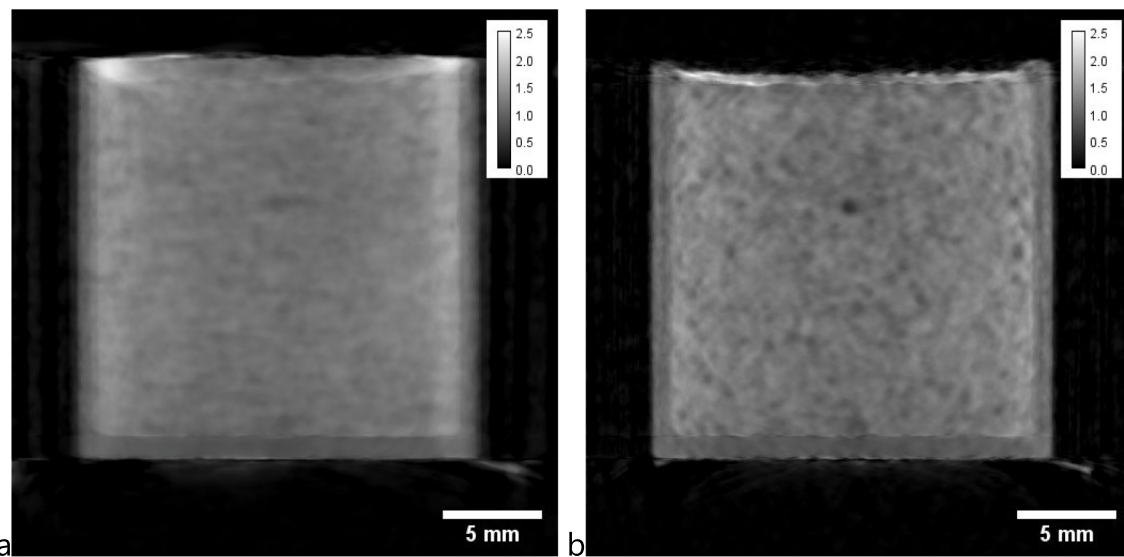
Fig. 3. Analogous results as in Fig. 2 but obtained from the neutron tomograms. The greyscale corresponds to the neutron linear attenuation coefficient in [cm^{-1}]. Owing to the high attenuation of the neutron beam by hydrogen, brighter regions have higher content of water (or, at the surface, paraffin wax).

Materials) is the vertical displacement of the mortar samples. This deformation is quantified later on. Another important feature is that the loss of water manifested in the decrease of voxel value is not uniform in the samples. It is especially pronounced in the zones near the sides of the samples, particularly for the REF and CURE-MIX mortars. This is related also to the initial distribution of the voxel values in the specimens' volumes. It can be seen in Fig. 3 at early age (15 min from casting) and in the left column in Fig. S2 in Supplementary Materials that the regions near to the walls of the container are brighter, i.e. have higher neutron attenuation coefficient, than the central part.

Although a monotonic increase in the neutron attenuation signal toward the peripheries of the samples often occurs because of the so-called scattering artifact, and to a lesser extent, the beam-hardening artifact [42,52,53], the authors believe that these artifacts are only partially responsible for the increasing voxel values toward the peripheries. This is because there is no visible continuous and gradual decrease in voxel value from the boundaries to the center of the specimen. Rather, the very bright regions are confined to the shallow sub-surface of the lateral boundaries.

The higher initial water content is likely in part due to a higher cement paste content near the walls of the specimen's holder. The phenomenon of increased paste content close to the walls is well-known for concrete [54,55]. According to a model derived from the numerical simulations in [54], a region of about 0.3 mm near the walls should be characterized by a decreased concentration of the aggregates, thus higher cement paste content. Further, detachment of the mortar from the walls of the container would amplify water collection and migration along such interfaces during drying.

Another important observation is that the regions along the vertical peripheries of the specimens lose voxel values over time gradually starting from the top. This reflects the gradual drying of the samples starting from the top surface.

As long as the REF and CURE-MIX samples are qualitatively similar, clearly distinct features could be observed for the CURE-SURF mortar. This mortar lost significantly less water and the drying was uniform in the sample. This is undoubtedly due to the film of paraffin-based curing compound present on the top surface. A distinct layer of thickness of about 1 mm can be seen in the initial tomogram, see Fig. 3a (and also
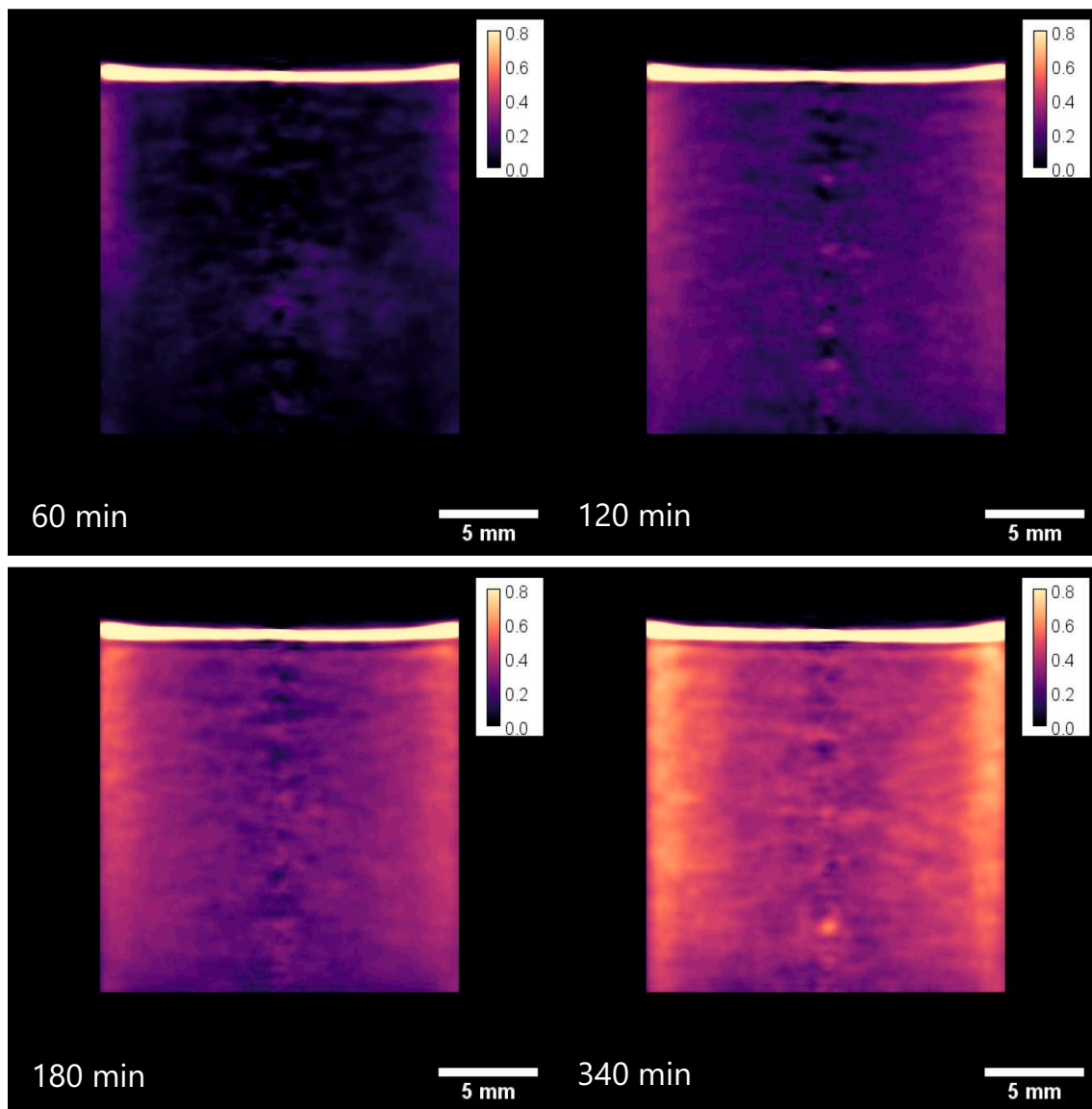
Fig. 4. Difference images of the cylindrically averaged neutron tomograms for the REF mortar at 60, 120, 180, 340 min from casting (with respect to the first tomogram at 15 min from casting). The Magma color scale [69] represents the change of the neutron linear attenuation coefficient, μ_n, in [cm^{-1}]. Higher values correspond to higher water loss. The color scale was cropped at 0.0 (mass gain was neglected) and 0.8 (above this threshold the loss in μ_n was due to displacement of the whole mortar body rather than loss of water from within the mortar).

bottom row in Fig. S2 in the Supplementary Materials). Note that the estimated thickness of the paraffin compound was about 0.8 mm. It is however possible that this layer was additionally fed by the bleeding water accumulating at the top. In the tomogram collected at the end of the experiment, a thin bright layer can be seen at the top of the mortar, see Fig. 3b. This layer with high neutron attenuation is due to now densified paraffin wax remaining as water evaporated from the curing compound.

3.2. Quantification – mass loss and settlement

In Fig. 7, mass loss per unit area of the drying surface measured with a balance is presented for mortars and compared to that of pure water and pure paraffin-based curing compound (the two liquids were placed in the PTFE holders and exposed to drying near the actual mortar specimens). The evaporation of the free water surface was equal to about 0.55 kg/m^2/h. This value is close to the estimations made based on a nomogram available in the recommendation ACI 305R [56].

A much lower evaporation rate was observed for the paraffin-based dispersion and it was almost exclusively due to water evaporation (evaporation of the paraffin wax itself is several orders of magnitude slower [57]).

The time interval of about 6 h between the first (zero point) and the second measurements for the mortars corresponds to the time in which the samples were measured with tomography. The total amount of water evaporated during the first 6 h of drying from mortars REF and CURE-MIX is almost identical to that evaporated from the free water surface. The CURE-SURF mortar with paraffin-based compound spread on the surface had mass loss of about 40% of that measured for the REF and CURE-MIX mortars.

After about 6 h, the rate of evaporation decreases considerably. Note that the lines in Fig. 7 are plotted only as a visual aid – the actual course of the mass loss curves in between the points was not necessarily linear. More on the course of the mass loss trends is revealed from the neutron data later in this section.

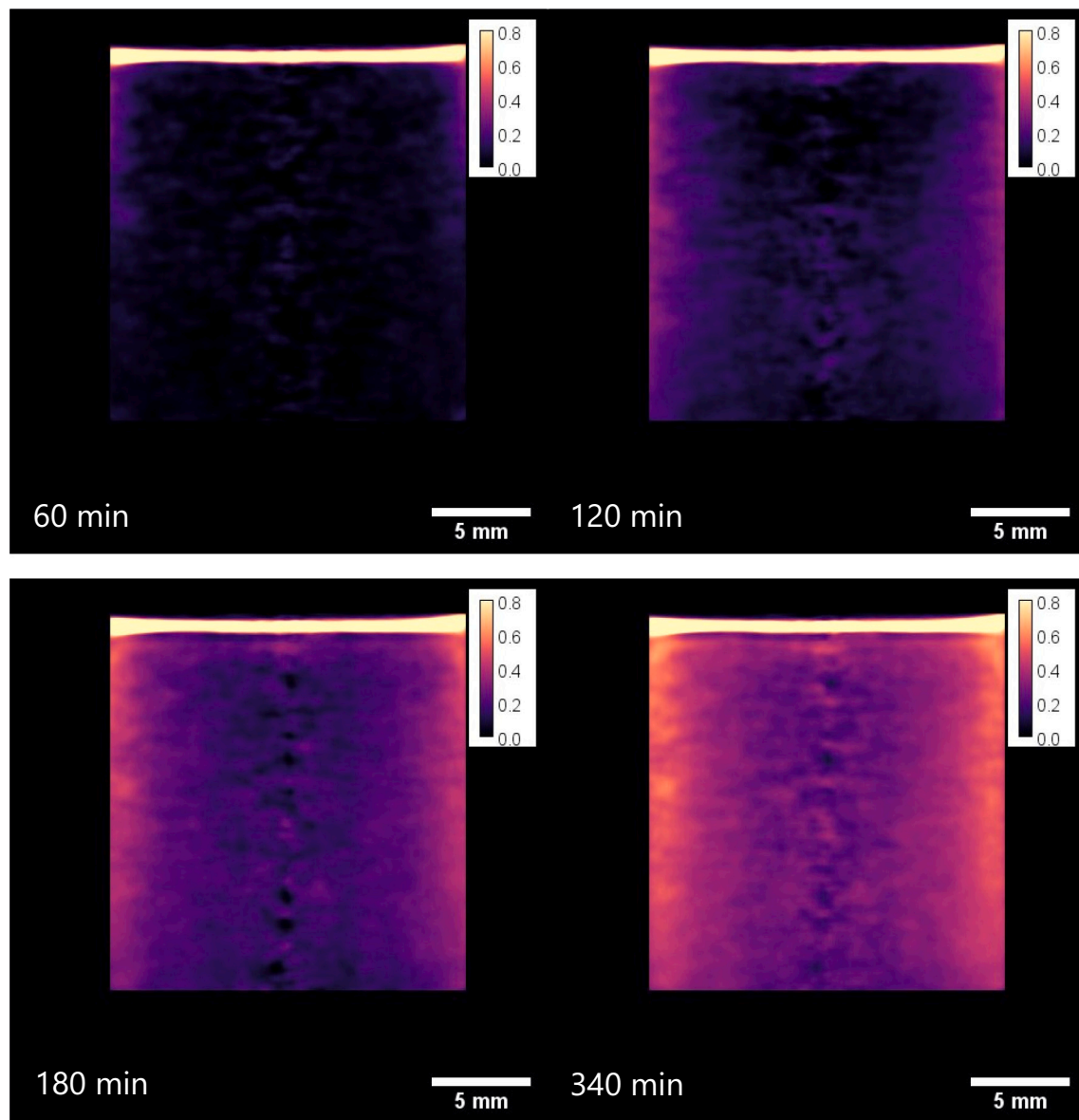As pointed out in the Introduction, the high contrast due to hydrogen

Fig. 5. Difference images – CURE-MIX mortar (for details see caption of Fig. 4).

in neutron images enables to follow almost quantitatively the change in bulk water content and the spatial distribution of the water in the mortars. All the following tomography results (both water content changes and settlements) are referred to the scan at 15 ± 1 min from casting.

The theoretical neutron attenuation coefficients calculated in Section 2.3 (about 1.4 cm^{-1}, see also Section S3 in Supplementary Materials) are in a reasonable agreement with those actually measured - the average voxel value in the REF and CURE-MIX mortars was equal to 1.36 cm^{-1} and in the REF-duplicate and CURE-SURF mortar it was 1.28 cm^{-1}. Besides the uncertainties related to the corrections and quantification procedures, the lower voxel values measured during the first tomography compared to those estimated theoretically might be partially due to the loss of water from the samples before the tomographic scans started (15 min after casting and about 5–10 min after exposure to the air flow). The measured changes of voxel values were transformed into changes in water content and integrated over the whole volume of the mortar to represent total changes of water content, Fig. 8. It should be stressed here that the deformations of the mortar volume played an important role in the calculations of the water loss – the total integrated signal was

decreasing due to decreasing voxel value in different voxels, but also due to the significant reduction of volume of the whole mortar. This was in particular important for the CURE-SURF mortar. In this mortar, the mass change is due to both loss of water from the bulk of the mortar and from the layer of curing compound poured on the surface. In fact, the curing compound experiences significant drying itself (see light-blue dashed line with empty diamond markers in Fig. 7). Of the 0.18 g of the paraffin-based dispersion applied on the surface, about 0.11 g was nominally water. Hence, it can be assumed that the total water loss from the CURE-SURF mortar of 0.35 g was partially due to the water loss from the curing compound (0.11 g) and partially due to water loss from the bulk of the mortar (0.24 g).

It can be seen that the mass loss estimated from the neutron tomography is lower than the actual mass loss determined with the gravimetric measurements (see single empty markers around 360 and later). However, the trend for different mortars is the same. The results for the replicate REF specimens are in a good agreement, with a slightly slower mass loss for the REF-duplicate specimen after 60 min. The mass loss rate of the CURE-MIX mortar appears to be slightly lower compared to the REF mortars. This difference may be however statistically
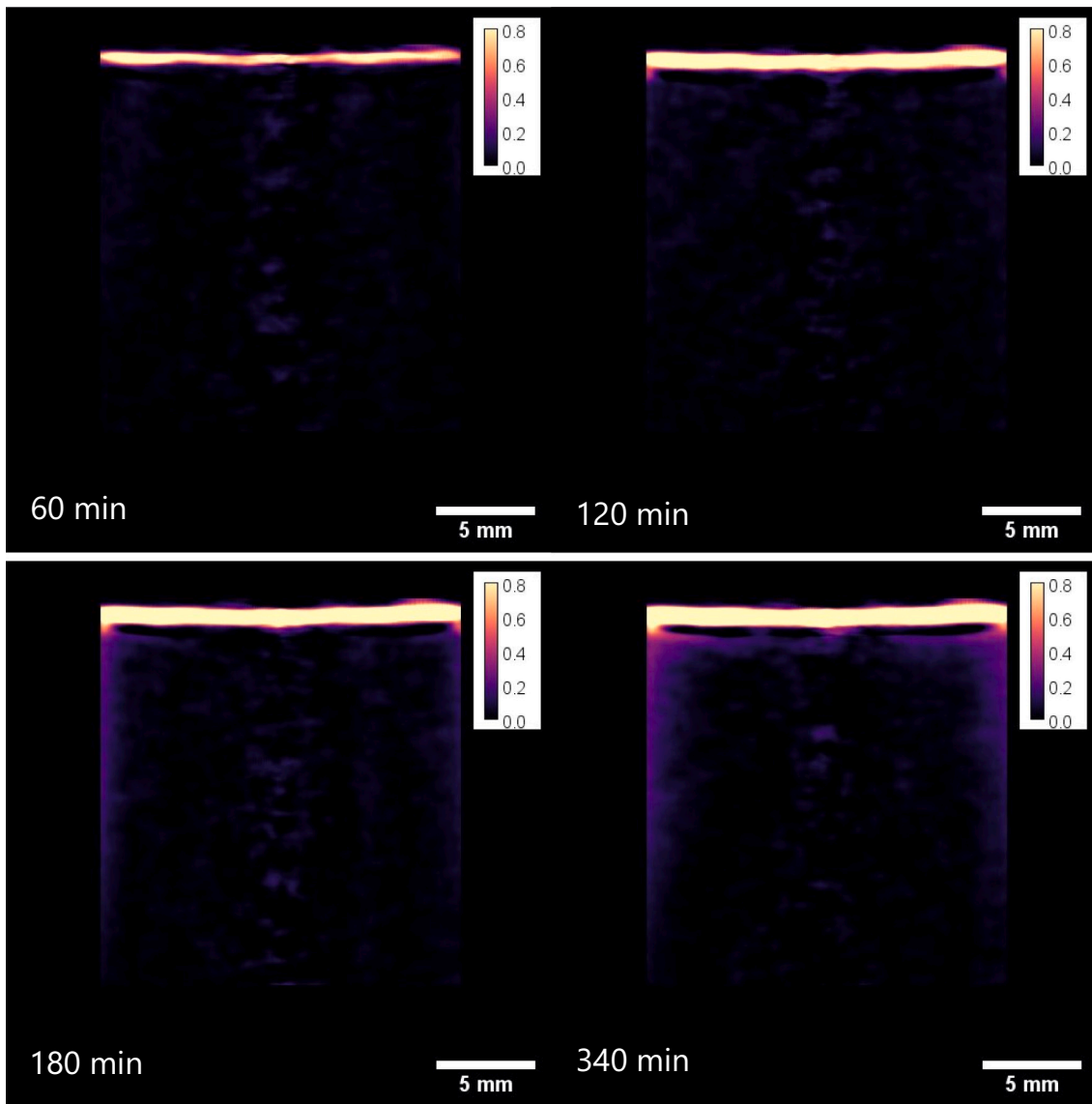
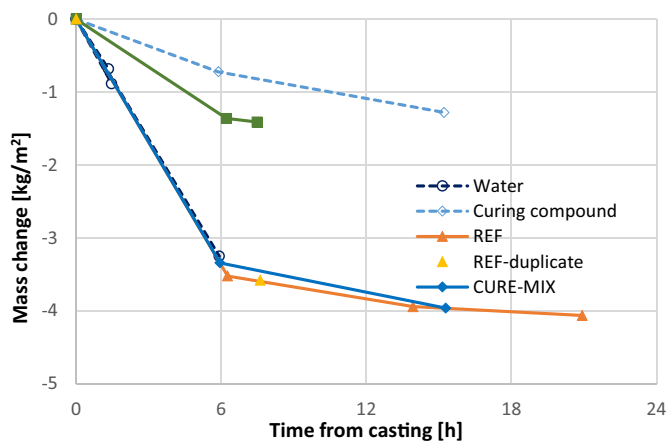**Fig. 6.** Difference images – CURE-SURF mortar (for details see caption of Fig. 4).

Fig. 7. Mass change of cylindrical mortar samples determined with a balance before the tomographic scans (zero time) and at later time instants. The mass loss was divided by the nominal surface area of the cylindrical samples exposed to drying (top surface), 2.545 cm^2. The mass loss from the sample holders filled with deionized water and paraffin-based curing compound was measured too.
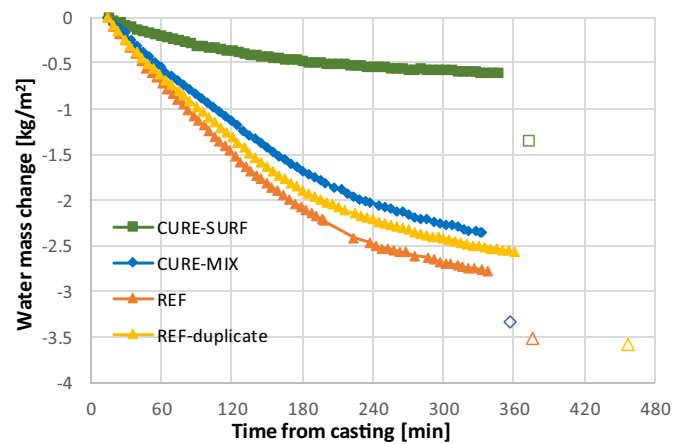
Fig. 8. Water mass change (filled markers) estimated based on the changes of voxel values in neutron tomograms (representing neutron linear attenuation coefficient) and integrated over the whole volume of the specimens compared to the gravimetric measurements (empty markers).

insignificant considering the scatter of the REF specimens.

The results in Fig. 8 also show that the initial approximately linear trend of mass loss slightly slows down at around 60 min and later more significantly from about 180 min. These changes can be better assessed based on the calculated rates presented in the Supplementary Materials, Fig. S3.

After obtaining a binary mask of the mortar specimens based on image segmentation, the deformations of the mortar specimens could be followed. The deformations of a mortar right after casting and before percolation of solids, referred to as the set, occur exclusively along the vertical direction (settlement). After the setting time, the vertical and horizontal deformations occurring due to bulk shrinkage should be in principle equal [31]. However, the small magnitude of the shrinkage that develops after the initial steep deformation (after about 60 min from casting for the REF and CURE-MIX mortars) makes the exact quantification of the horizontal deformations impossible. At the time instant when the vertical strains stopped, a detachment of the mortar from the walls of the cylindrical sample holder occurred in some regions of the specimens. It is however also possible that the detachment from the walls had occurred earlier but had been masked by the high signal due to water present on the interfaces that first disappeared around 60 min.

It could be observed that the displacements near the walls of the sample holder are to a certain extent hindered. In order to avoid this boundary effect, the displacements of the top surface in a central circular region of interest with diameter of 12 mm were averaged, hence disregarding the ~3 mm ring near the walls. The average vertical displacements of the top surface (settlement) based on both the X-ray and the neutron tomograms are presented in Fig. 9. A good agreement

Fig. 9. Average vertical displacement (settlement) of the top surface of the mortars obtained from a) X-ray and b) neutron tomography.

between the REF and REF-duplicate specimens was again obtained, and the only remarkable difference was a shift of about 70 μm in the initial steep part of the settlement evaluated with the neutrons, see orange markers in Fig. 9b.

Lower vertical displacements were found with X-rays than with neutrons, although the kinetics is very similar between the two irradiation modes. Mind that the X-ray tomography data were characterized by a lower contrast at the top interface and hence higher scatter compared to neutrons. The lower deformations resolved by the X-ray are to be expected – the X-rays tomography was sensitive to the dense solids and less sensitive to the water-rich cement paste layer near the surface or bleeding water accumulated at the top. On the other hand, the total deformation resolved by the neutron tomography includes the displacement of the top surface of the bleeding water that evaporates rapidly at early stages of drying. The difference between the two tomography modes was especially pronounced for the CURE-SURF mortar, where the settlement resolved with the neutrons was about 370 μm higher than with X-rays. In fact, the loss of the 0.11 g of water present initially in the curing compound spread over a surface of about 2.5 cm^2 would correspond to a settlement of the layer of the compound of as much as 430 μm. This shows that the higher deformations of the neutron tomography are primarily due to the layer of bleeding water accumulated on the mortar surface and evaporating in the initial 1 h (for the REF and CURE-MIX) or 2 h (for the CURE-SURF) of drying. The smaller difference between the X-ray and neutron settlements than the estimated 430 μm (for CURE-SURF) also suggests that the X-ray tomography may have to a certain extent overestimated the actual settlement of the solid part of the mortars. This is possible considering the low contrast visible on the top surface in the X-ray tomography, see Fig. 2.

Both specimens of the reference mortar (REF and REF-duplicate) seem to have had a slightly faster displacement rate than the CURE-MIX mortar in the initial 60 min from casting (also in line with the mass loss results in Fig. 8), as assessed both based on the X-ray and neutron tomograms. After this time, the displacements were almost identical. A clearly different trend was observed for the CURE-SURF mortar. The vertical settlement proceeded slower and the initial steeper part of the deformation continued for at least 180 min. The final displacement of the CURE-SURF mortar resolved by the X-ray tomography was slightly higher (up to about 100 μm) than for the other two mortars. A much higher difference in final displacement was found with neutrons, where the top surface of the CURE-SURF mortar settled about 280 μm more than of the other two mortars. This can be explained again by the evaporation of water from the curing compound that amplified the settlement resolved with neutron tomography.

4. Discussion

The results of the time-lapse, bimodal neutron/X-ray tomography measurements presented here are particularly interesting with regard to: 1) the mechanisms of plastic shrinkage, and 2) the mechanisms by which the curing compounds work. The following discussion is devoted to these two aspects, respectively.

4.1. Mechanisms of plastic shrinkage

The water mass loss from fresh mortars during evaporation undergoes two main stages: a constant rate period (CRP), followed by a falling rate period (FRP). These two stages were related to an initial period of constant permeability of a saturated mortar followed by a period of decreasing permeability [31,58,59].

From the water mass loss (Fig. 8) and its rate (Fig. S3 in the Supplementary Materials) estimated with neutron tomography, it appears that during the first 60 min the evaporation rate from the REF and CURE-MIX mortars remains at a fairly constant, high level. Hence, it could be assumed that this period corresponds to the CRP. It is however
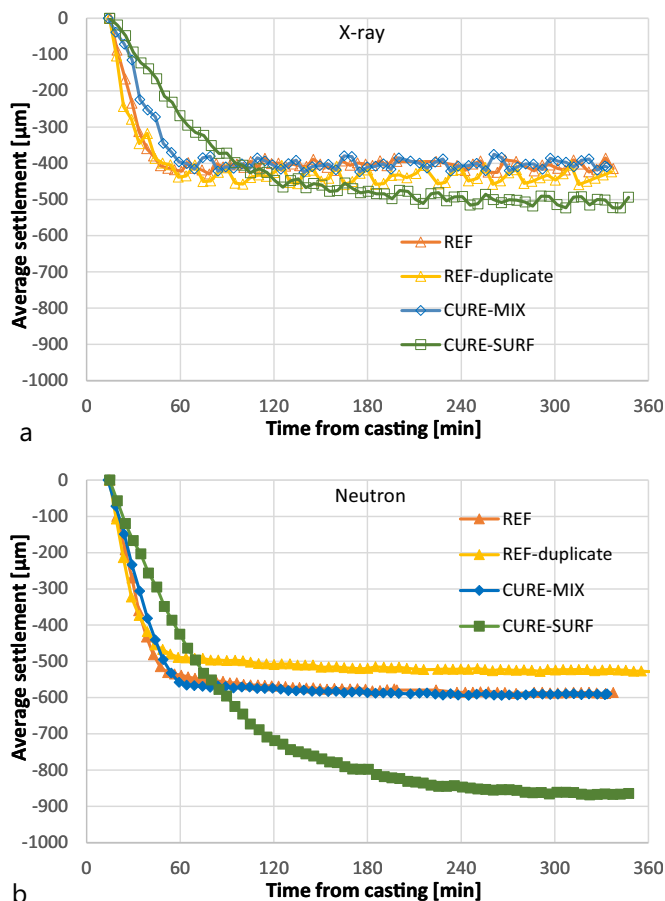
possible that a slow drop of the high evaporation rate started already earlier on – this uncertainty stems from the high scatter of the estimated mass loss rates and the time at which the measurements started (only after about 15 min from casting). After about 60 min from casting, a slight reduction of the evaporation rate is observed, which becomes more significant after about 120–180 min.

The reduction of the evaporation rate occurs when water is not transported to the drying surface at a sufficient rate and is related to the reduction of the effective permeability [31,59]. This in turn can be in a general case caused by two processes - cement hydration and partial desaturation of pores. The former will result in reduction of the intrinsic permeability as the pores are gradually filled with the hydration products of cement. However, in the particular case studied here, considering the early stage of the hydration process (dormant period), the contribution of cement hydration (and of the reduction of intrinsic permeability that it causes) to the early onset of the falling rate period at about 60–120 min can be excluded. It is however possible that it contributed to the reduction of the mass loss rate after about 180 min. The second contribution to the reduced effective permeability, desaturation of pores, will lead to reducing the efficiency of the advective transport of water in the (partially emptied) pores where water paths become discontinuous. This process can be quantified by means of the relative permeability [60].

The penetration of air into the pore system (desaturation) of a granular medium like mortar during evaporation occurs after reaching a certain value of the capillary pressure, referred to as the air entry pressure. This is a consequence of reaching a sufficiently high stiffness to support the emptying of pores of water [31,61–63]. Before this threshold, the volumetric water content remains fairly constant and corresponds to a saturation degree equal to 1 even though the material loses water by evaporation [61]. This is because the loss of water translates fully to the bulk deformation of the body of a (not sufficiently stiff) mortar. This is well illustrated when the average settlement of the top surface of a mortar is compared to the settlement estimated from water mass loss (the latter in turn estimated from changes in neutron voxel value), see e.g. for the REF mortar in Fig. 10.

It can be hence estimated that the air entry occurred likely before 60 min from casting. Even after the air entry, there can be still a (rather short) period when the transport of water to the surface is efficient enough to keep up with the evaporation rate and the mortar thus remains in the CRP regime. As the desaturation of pores and breaking of water paths progresses, the water supply decreases beyond that stipulated by the evaporation rate and as soon as the accumulated surface

water evaporates, the FRP starts [64]. Because of the small sizes of the samples studied here, the transition from the CRP to the FRP was most likely very fast.

At the same time, it could be observed that the initial steep deformation slowed down after about 45 min from casting and became all but arrested within about next 15 min, see Figs. 9 and 10. After this time, the vertical deformations increase on average by a very small magnitude, close to the voxel size. These characteristic time instants of the deformations are in line with those of the water loss. The ceasing of the fast deformation period during evaporation is a consequence of a rapid increase of stiffness of the mortars. In general, the stiffness increases because of the percolation of solids in the mortar. In the particular conditions tested here, this percolation is not (yet) caused by the hydration process of cement – as mentioned earlier, after only 60 min cement hydration should be still in the dormant period. Instead, the stiffening manifested in rapid ceasing of deformations occurs so early likely due to the consolidating action of capillary pressure triggered by early drying and amplified by the small size of the specimens. Such consolidation-driven stiffening is well known for soils [65] and was also proposed for concrete by Radocea [2]. Capillary pressure stiffening was shown in [6,31] to be one of the major factors triggering plastic shrinkage cracking. According to the experiments and the modelling study presented in [6,31], with the onset of capillary pressure buildup, a rapid increase of the bulk modulus of mortars by a factor of about 6 takes place within a relatively short time period (about 20 min).

It should be stressed again that the samples tested in the present study were indeed very small – the height of the samples was only 19 mm (compared to samples with depths of several centimeters or more in [6,31,58,62]). Hence, considering the small capacity of bleeding water and relatively fast drying, the percolation of solids with the corresponding onset of capillary pressure stiffening and the air entry occurred very early and the time span (in the range of minutes) in which these processes arrest the deformations was significantly shorter compared to larger samples. This observation is in line with the measurements of capillary pressure in samples of different depth presented in [2] or with the measurements of bleeding presented in [66].

4.2. Action of curing compounds

The curing compound based on paraffin dispersion is aimed at reducing the evaporation of water from concrete by sealing off its drying surface [17,21,67]. As discussed in the introduction, this can happen either when the curing compound is applied directly on the drying surface, or when it is added to the mix and then the sealing agent accumulates near the drying surface and gradually seals it. In the tests, slower mass loss in the mortar with mixed-in curing compound was observed, however it is not clear how much of such difference comes from intrinsic variability of the mixtures and environmental conditions. In any case, no significant effect on the deformations was observed. This limited (or no) action was most likely due to an insufficient amount of the curing compound used. Even though the maximum amount recommended by the producer was applied, it should be stressed that the mortar specimen was very shallow. The amount of curing compound that can migrate to the drying surface and accumulate there in the constant rate evaporation period is proportional to the depth of the drying element. In other words, in the present tests the absolute amount of the curing compound (and water to carry it) that could migrate from the underlying depth of 19 mm was insufficient to assure a sufficient sealing of the drying surface. In fact, the mass of curing compound nominally present in the sample was approximately 0.05 g only. This translates to about 0.2 kg per m^2 of the cured surface and is considerably less than used in previous studies, e.g. 0.7 kg/m^2 in [17] or 0.5 kg/m^2 in [14]. In the case of surface application (CURE-SURF), about 0.7 kg/m^2 was used. The amount mixed in the CURE-MIX mortar could not be increased beyond the limit of 1.5% (by mass of cement) recommended by the producer as it could have adverse effects on e.g. hydration of
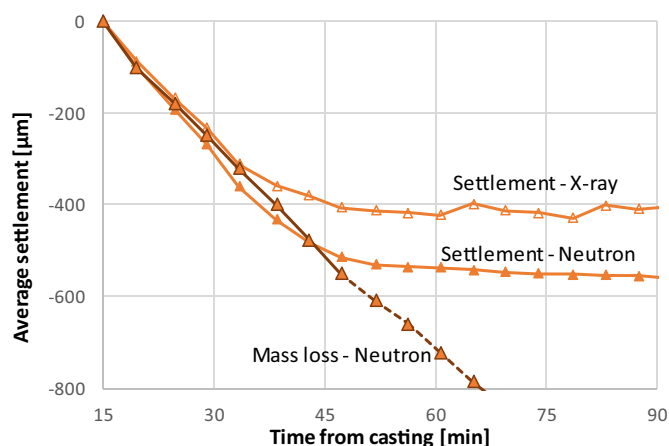
Fig. 10. Average vertical displacement (settlement) of the top surface of the REF mortar obtained from X-ray and neutron tomography compared to the settlement estimated based on water mass loss (from neutron data). The dashed part of the mass loss line refers to the period where the settlement estimation was no longer valid (settlement all but ceased).

cement or could affect the consolidation process of the mortar. Based on the previous tests [14,17], it can be assumed that the curing compound should be efficient in limiting evaporation for mortar or concrete layers of realistic thickness (above around 8 cm, assuming that all paraffin can migrate to the surface). In the extreme case that all curing compound migrates to the surface, the CURE-SURF mortar could be in fact considered as a model ideal case also for the curing compound used as admixture.

On the other hand, a very clear effect of the relatively large amount of the paraffin-based dispersion spread directly on the top surface was observed. The mass loss from the mortar estimated with neutron tomography decreased significantly, to about 23% of that observed for the REF mortars. Considering that a large part of the mass loss in fact was due to the water evaporation from the curing dispersion itself, this percentage reduces for the mortar itself to only 9%. The evaporation of water from the dispersion was also responsible for the large deformation observed with neutrons – the settlement resolved with the neutrons was in large part due to the evaporation of water from the layer of the curing compound on the surface. Along with the retarded evaporation of water, the rate of vertical displacement was considerably reduced in the CURE-SURF mortar. At the same time, the initial deformation stage lasted longer than in the REF or CURE-MIX mortar, until about 3 h. This can be explained as an effect of the delayed capillary-pressure stiffening and air entry discussed in the previous section. In fact, delays in apparent setting time were previously reported for samples that were kept sealed compared to those exposed to drying [31]. In the ideal case of curing, the layer of the curing compound should seal the surface and protect it from evaporation until percolation caused by the hydration of cement can arrest the deformations and eliminate cracking. Although the relatively large vertical displacement observed in the CURE-SURF mortar could be detrimental in terms of cracking caused by differential settlement (e.g., over reinforcing bars or change of the section depth in large concrete elements) [68], it does not result in the buildup of restraint stresses, as the material is still not consolidated. On the other hand, in the mortars without curing, the high early stiffness caused by capillary pressure stiffening in absence of hydration-driven strength could lead to serious cracking if the deformations were restrained.

5. Conclusions

The results presented here show that the combination of simultaneous X-ray and neutron tomography is a powerful technique for following the water loss of mortars exposed to early drying and the corresponding plastic shrinkage. Further broad applications could be in porous materials were the solid skeleton and the contained fluid(s) cannot be resolved simultaneously with either of the methods alone. A typical case is fluid transport in porous solids like concrete, soil, ceramics etc.

The displacements of the drying mortar resolved with both methods ceased after about 1 h. This arrest of deformations occurred considerably earlier than could be expected from hydration of cement. The reason for such early consolidation was the so-called capillary pressure stiffening and air entry occurring on the onset of emptying of pores by drying. These processes occurred very early and within a short time window due to the small size of the samples and hence very rapid drying.

The particular focus of the presented study was on the performance of curing with a sealing membrane. To this end, a commercial curing compound based on paraffin dispersion was applied in two ways: either mixed in the mortar, or poured onto the top surface after casting. Although slightly slower mass loss was determined for the mortar with mixed-in curing compound, the total deformations were similar to the reference mortars with no curing. This limited effect was most likely due to the insufficient amount of the curing compound available in the miniature specimen. It should be stressed that the amount of the curing compound that can accumulate and seal the drying surface is proportional to the depth of the underlying concrete – the 19-mm deep samples

were too shallow to represent field conditions for this particular case. On the other hand, the mortar with curing compound spread onto the top surface experienced significantly lower (even as much as 10 times lower based on neutron tomography analysis) mass loss and also much slower vertical displacement (settlement). As the water from the paraffin-dispersion evaporated, the curing compound formed a clearly visible densified layer of paraffin wax on the drying surface. A further effect of the reduced evaporation was that the settlement continued longer as it was not arrested by capillary-pressure stiffening and air entry. This effect could be considered as positive, assuming that the sealing action would continue until setting and until strength gain caused by cement hydration.

CRediT authorship contribution statement

Declaration of competing interest

The authors declare no conflict of interest.

Acknowledgements

Appendix A. Supplementary data

Supplementary data to this article can be found online at https://doi.org/10.1016/j.cemconres.2020.106289.

References

[1] W. Lerch, Plastic shrinkage, in: ACI Journal Proceedings, ACI, 1957.
[2] A. Radocea, A model of plastic shrinkage, Mag. Concr. Res. 46 (167) (1994) 125–132.
[3] M.D. Cohen, J. Olek, W.L. Dolch, Mechanism of plastic shrinkage cracking in portland cement and portland cement-silica fume paste and mortar, Cem. Concr. Res. 20 (1) (1990) 103–119.
[4] V.T.N. Dao, P.F. Dux, P.H. Morris, L. O'Moore, Plastic shrinkage cracking of concrete, Aust. J. Struct. Eng. 10 (3) (2010) 207–214.
[5] K. Kovler, S. Zhutovsky, Overview and future trends of shrinkage research, Mater. Struct. 39 (9) (2006) 827–847.
[6] S. Ghourchian, M. Wyrzykowski, M. Plamondon, P. Lura, On the mechanism of plastic shrinkage cracking in fresh cementitious materials, Cem. Concr. Res. 115 (2019) 251–263.
[7] F. Ghasemzadeh, M. Pour-Ghaz, Effect of damage on moisture transport in concrete, J. Mater. Civ. Eng. 27 (9) (2015), 04014242.
[8] V. Slowik, M. Schmidt, A. Neumann, J. Dorow, Early age cracking and its influence on the durability of concrete structures, Proceedings of the 8th International Conference on Creep, Shrinkage and Durability of Concrete and Concrete Structures-CONCREEP (2008) 471–477.
[9] S. Ephraim, George A. Malchow, Jr., Studies on Control of Durability of Concrete Through Proper Curing, ACI Symposium Publication 100.
[10] C.C. Rhodes, Curing concrete pavements with membranes, ACI Journal Proceedings 47 (12) (1950).
[11] E. Senbetta, Curing and Curing Materials, Significance of Tests and Properties of Concrete and Concrete-Making Materials, ASTM International, 1994.

[12] C. Nmai, R. Tomita, F. Hondo, J. Buffenbarger, Shrinkage-reducing admixtures, Concr. Int. 20 (4) (1998) 31–37.

[13] D.P. Bentz, M.R. Geiker, K.K. Hansen, Shrinkage-reducing admixtures and early-age desiccation in cement pastes and mortars, Cem. Concr. Res. 31 (7) (2001) 1075–1085.

[14] S. Ghourchian, M. Wyrzykowski, L. Baquerizo, P. Lura, Performance of passive methods in plastic shrinkage cracking mitigation, Cem. Concr. Compos. 91 (2018) 148–155.

[15] P. Lura, G.B. Mazzotta, F. Rajabipour, J. Weiss, K. Kovler, Evaporation, settlement, temperature evolution, and development of plastic shrinkage cracks in mortars with shrinkage-reducing admixtures, Int. RILEM-JCI Seminar on Concrete Durability and Service Life Planning (ConcreteLife'06), 2006.

[16] P. Lura, B. Pease, G.B. Mazzotta, F. Rajabipour, J. Weiss, Influence of shrinkage-reducing admixtures on development of plastic shrinkage cracks, ACI Mater. J. 104 (2) (2007) 187–194.

[17] A. Leemann, P. Nygaard, P. Lura, Impact of admixtures on the plastic shrinkage cracking of self-compacting concrete, Cem. Concr. Compos. 46 (0) (2014) 1–7.

[18] J. Saliba, E. Rozière, F. Grondin, A. Loukili, Influence of shrinkage-reducing admixtures on plastic and long-term shrinkage, Cem. Concr. Compos. 33 (2) (2011) 209–217.

[19] J. Wang, R.K. Dhir, M. Levitt, Membrane curing of concrete: moisture loss, Cem. Concr. Res. 24 (8) (1994) 1463–1474.

[20] R.K. Dhir, M. Levitt, J. Wang, Membrane curing of concrete: water vapour permeability of curing membranes, Mag. Concr. Res. 41 (149) (1989) 221–228.

[21] C. Rhodes, J.R. Evans, An Appraisal of the Membrane Method of Curing Concrete Pavements, Michigan State Highway Department 1948.

[22] R.F. Blanks, H.S. Meissner, L.H. Tuthill, Curing concrete with sealing compounds, ACI Journal Proceedings 42 (4) (1946).

[23] C. ASTM, 309-Standard Specification for Liquid Membrane-forming Compounds for Curing Concrete, American Concrete Institute, 1998.

[24] M.S.R. Chand, P.S.N.R. Giri, G.R. Kumar, P.R. Kumar, Paraffin wax as an internal curing agent in ordinary concrete, Mag. Concr. Res. 67 (2) (2015) 82–88.

[25] M. Maslehuddin, M. Ibrahim, M. Shameem, M.R. Ali, M.H. Al-Mehthel, Effect of curing methods on shrinkage and corrosion resistance of concrete, Constr. Build. Mater. 41 (2013) 634–641.

[26] J.P. Liu, L. Li, C.W. Miao, Q. Tian, Q.P. Ran, Y.J. Wang, Reduction of water evaporation and cracks on plastic concrete surface by monolayers, Colloids Surf. A Physicochem. Eng. Asp. 384 (1) (2011) 496–500.

[27] R. Henkensiefken, P. Briatka, D.P. Bentz, T.E. Nantung, J. Weiss, Plastic shrinkage cracking in internally cured mixtures, Concr. Int. 32 (2) (2010) 49–54.

[28] ASTM, C1579-13 Standard Test Method for Evaluating Plastic Shrinkage Cracking of Restrained Fiber Reinforced Concrete (Using a Steel Form Insert), ASTM International, West Conshohocken, PA, 2013.

[29] S. Ghourchian, M. Wyrzykowski, L. Baquerizo, P. Lura, Susceptibility of Portland cement and blended cement concretes to plastic shrinkage cracking, Cem Concr Compos 85 (Supplement C) (2018) 44–55.

[30] C. Qi, J. Weiss, J. Olek, Characterization of plastic shrinkage cracking in fiber reinforced concrete using image analysis and a modified Weibull function, Mater. Struct. 36 (6) (2003) 386–395.

[31] S. Ghourchian, M. Wyrzykowski, P. Lura, A poromechanics model for plastic shrinkage of fresh cementitious materials, Cem. Concr. Res. 109 (2018) 120–132.

[32] D.P. Bentz, K.K. Hansen, Preliminary observations of water movement in cement pastes during curing using X-ray absorption, Cem. Concr. Res. 30 (7) (2000) 1157–1168.

[33] D.P. Bentz, K.K. Hansen, H.D. Madsen, F. Vallée, E.J. Griesel, Drying/hydration in cement pastes during curing, Mater. Struct. 34 (9) (2001) 557–565.

[34] P. Zhang, F.H. Wittmann, P. Lura, H.S. Müller, S. Han, T. Zhao, Application of neutron imaging to investigate fundamental aspects of durability of cement-based materials: a review, Cem. Concr. Res. 108 (2018) 152–166.

[35] F.C. de Beer, W.J. Strydom, E.J. Griesel, The drying process of concrete: a neutron radiography study, Appl. Radiat. Isot. 61 (4) (2004) 617–623.

[36] C. Villani, C. Lucero, D. Bentz, D. Hussey, D.L. Jacobson, W. Weiss, Neutron Radiography Evaluation of Drying in Mortars With and Without Shrinkage Reducing Admixtures, American Concrete Institute Fall Meeting, Washington, DC, 2014.

[37] P. Zhang, F.H. Wittmann, T. Zhao, E. Lehmann, Z. Jin, Visualization and quantification of water movement in porous cement-based materials by real time thermal neutron radiography: theoretical analysis and experimental study, SCIENCE CHINA Technol. Sci. 53 (5) (2010) 1198–1207.

[38] M. Wyrzykowski, P. Trtik, B. Münch, J. Weiss, P. Vontobel, P. Lura, Plastic shrinkage of mortars with shrinkage reducing admixture and lightweight aggregates studied by neutron tomography, Cem. Concr. Res. 73 (0) (2015) 238–245.

[39] E. Roubin, E. Andò, S. Roux, The colours of concrete as seen by X-rays and neutrons, Cem. Concr. Compos. 104 (2019) 103336.

[40] E.H. Lehmann, P. Vontobel, N. Kardjilov, Hydrogen distribution measurements by neutrons, Appl. Radiat. Isot. 61 (4) (2004) 503–509.

[41] A.P. Kaestner, P. Trtik, M. Zarebandkouki, D. Kazantsev, M. Snehota, K.J. Dobson, E.H. Lehmann, Recent developments in neutron imaging with applications for porous media research, Solid Earth Discussions 7 (4) (2015) 3481–3510.

[42] P. Vontobel, E.H. Lehmann, R. Hassanein, G. Frei, Neutron tomography: method and applications, Phys. B Condens. Matter 385–386 (2006) 475–480.

[43] P. Trtik, B. Münch, W.J. Weiss, A. Kaestner, I. Jerjen, L. Josic, E. Lehmann, P. Lura, Release of internal curing water from lightweight aggregates in cement paste investigated by neutron and X-ray tomography, Nuclear Instruments and Methods in Physics Research Section A: Accelerators, Spectrometers, Detectors and Associated Equipment 651 (1) (2011) 244–249.

[44] P. Lura, M. Wyrzykowski, C. Tang, E. Lehmann, Internal curing with LWA produced from biomass-derived waste, Cem. Concr. Res. 59 (2014) 24–33.

[45] L. Josserand, F. de Larrard, A method for concrete bleeding measurement, Mater. Struct. 37 (10) (2004) 666.

[46] A.P. Kaestner, S. Hartmann, G. Kühne, G. Frei, C. Grünzweig, L. Josic, F. Schmid, E.H. Lehmann, The ICON beamline – a facility for cold neutron imaging at SINQ, Nuclear Instruments and Methods in Physics Research Section A: Accelerators, Spectrometers, Detectors and Associated Equipment 659 (1) (2011) 387–393.

[47] A.P. Kaestner, J. Hovind, P. Boillat, C. Muehlebach, C. Carminati, M. Zarebanadkouki, E.H. Lehmann, Bimodal imaging at ICON using neutrons and X-rays, Phys. Procedia 88 (2017) 314–321.

[48] A. Kaestner, E. Lehmann, M. Stampanoni, Imaging and image processing in porous media research, Adv. Water Resour. 31 (9) (2008) 1174–1187.

[49] G.R. Myers, A.M. Kingston, T.K. Varslot, M.L. Turner, A.P. Sheppard, Dynamic tomography with a priori information, Appl. Opt. 50 (20) (2011) 3685–3690.

[50] A. Kaestner, B. Münch, P. Trtik, L. Butler, Spatiotemporal computed tomography of dynamic processes, Opt. Eng. 50 (12) (2011) 123201.

[51] A. Hasegawa, H. Henriksson, F. Mompeán, C. Nordborg, Y. Rugama, E. Sartori, Nuclear data activities at the NEA Data Bank, in: Proceedings of the 2007 International Conference on Nuclear Data for Science and Technology-ND 2007, 2008.

[52] C. Carminati, P. Boillat, F. Schmid, P. Vontobel, J. Hovind, M. Morgano, M. Raventos, M. Siegwart, D. Mannes, C. Gruenzweig, P. Trtik, E. Lehmann, M. Strobl, A. Kaestner, Implementation and assessment of the black body bias correction in quantitative neutron imaging, PLoS One 14 (1) (2019), e0210300.

[53] P. Boillat, C. Carminati, F. Schmid, C. Grünzweig, J. Hovind, A. Kaestner, D. Mannes, M. Morgano, M. Siegwart, P. Trtik, P. Vontobel, E.H. Lehmann, Chasing quantitative biases in neutron imaging with scintillator-camera detectors: a practical method with black body grids, Opt. Express 26 (12) (2018) 15769.

[54] J.J. Zheng, C.Q. Li, M.R. Jones, Aggregate distribution in concrete with wall effect, Mag. Concr. Res. 55 (3) (2003) 257–265.

[55] P.C. Kreijger, The skin of concrete composition and properties, Mater. Constr. 17 (4) (1984) 275–283.

[56] D. ACI, 305R-Hot Weather Concreting, American Concrete Institute International, 1999.

[57] R.S. Bradley, A.D. Shellard, M.G. Evans, The rate of evaporation of droplets. III. Vapour pressures and rates of evaporation of straight-chain paraffin hydrocarbons, Proceedings of the Royal Society of London. Series A. Mathematical and Physical Sciences 198 (1053) (1949) 239–251.

[58] S. Ghourchian, M. Wyrzykowski, P. Lura, The bleeding test: a simple method for obtaining the permeability and bulk modulus of fresh concrete, Cem. Concr. Res. 89 (2016) 249–256.

[59] S. Ghourchian, Plastic Shrinkage Cracking in Concrete: From Mechanisms to Mitigation Strategies, ETH Zurich, 2018.

[60] M.T. van Genuchten, A closed-form equation for predicting the hydraulic conductivity of unsaturated soils, Soil Sci. Soc. Am. J. 44 (5) (1980) 892–898.

[61] G. Suazo, A. Fourie, J. Doherty, Experimental study of the evolution of the soil water retention curve for granular material undergoing cement hydration, J. Geotech. Geoenviron. 142 (7) (2016), 04016022.

[62] V. Slowik, M. Schmidt, R. Fritzsch, Capillary pressure in fresh cement-based materials and identification of the air entry value, Cem. Concr. Compos. 30 (7) (2008) 557–565.

[63] D.G. Fredlund, D. Sheng, J. Zhao, Estimation of soil suction from the soil-water characteristic curve, Can. Geotech. J. 48 (2) (2011) 186–198.

[64] S. Ghourchian, M. Wyrzykowski, P. Lura, A practical approach for reducing the risk of plastic shrinkage cracking of concrete, RILEM Technical Letters 2 (2017) 40–44.

[65] E.E. Alonso, A. Gens, A. Josa, A constitutive model for partially saturated soils, Géotechnique 40 (3) (1990) 405–430.

[66] M. Wyrzykowski, S. Ghourchian, S. Sinthupinyo, N. Chitvoranund, T. Chintana, P. Lura, Internal curing of high performance mortars with bottom ash, Cem. Concr. Compos. 71 (2016) 1–9.

[67] J. Plank, E. Sakai, C.W. Miao, C. Yu, J.X. Hong, Chemical admixtures—chemistry, applications and their impact on concrete microstructure and durability, Cem. Concr. Res. 78 (2015) 81–99.

[68] M.K. Moradllo, S.R. Reese, W.J. Weiss, Using neutron radiography to quantify the settlement of fresh concrete, Advances in Civil Engineering Materials 8 (1) (2019) 71–87.

[69] S. van der Walt, N. Smith, Matplotlib colormaps, Accessed, https://bids.github.io/colormap/. (Accessed 11 November 2020).